

## 2 **A Coupled Finite Difference Material Point Method and** 3 **Its Application in Explosion Simulation**

4 **X. X. Cui<sup>1</sup>, X. Zhang<sup>1, 2</sup>, X. Zhou<sup>3</sup>, Y. Liu<sup>1</sup> and F. Zhang<sup>1</sup>**

5 **Abstract:** The material point method (MPM) discretizes the material domain  
6 by a set of particles, and has showed advantages over the mesh-based methods  
7 for many challenging problems associated with large deformation. However, at  
8 the same time, it requires more computational resource and has difficulties to con-  
9 struct high order scheme when simulating the fluid in high explosive (HE) explo-  
10 sion problems. A coupled finite difference material point (CFDMP) method is  
11 proposed through a bridge region to combine the advantages of the finite difference  
12 method (FDM) and MPM. It solves a 3D HE explosion and its interaction with  
13 the surrounding structures by dividing the problem domain into FDM region and  
14 MPM region in space. FDM is employed to simulate the region where the detona-  
15 tion products disperse into the surrounding air, while the FSI region is simulated by  
16 MPM. A bridging region is employed to exchange the information. In the bridge  
17 region, MPM provides the boundary condition for FDM region by mapping the  
18 variables from MPM background grid nodes to FDM fictitious points, while FDM  
19 provides the boundary condition for MPM region by mapping the variables from  
20 FDM cell-centre points to MPM interface grid nodes. The transportation between  
21 the two computational regions is implemented by moving particles in the bridge re-  
22 gion. Numerical results are in good agreement with those of theoretical solutions,  
23 empirical formula and experiments. No obvious interface effect are observed in the  
24 bridge region in numerical tests.

25 **Keywords:** Material point method, finite difference method, bridge region, high  
26 explosive explosion, fluid-structure interaction.

---

<sup>1</sup> School of Aerospace, Tsinghua University, Beijing 100084, China.

<sup>2</sup> Corresponding author: xzhang@tsinghua.edu.cn

<sup>3</sup> Beijing Institute of Special Engineering Design and Research, Beijing 100028, China.

## 27 **1 Introduction**

28 A high explosive (HE) explosion is characterized by a number of challenging be-  
29 haviors including the highly pressurized product gas propagating into the quiescent  
30 surrounding air and the following fluid structure interaction (FSI) with the struc-  
31 tures nearby [Zukas and Walters (1998)]. So a lot of research have been carried out  
32 to study these kind of problems.

33 The traditional methods can be classified into Lagrangian method and Eulerian  
34 method based on the frame of reference [Benson (1992)]. The Lagrangian method  
35 has been widely used for structural analyses because of its capability of modeling  
36 history-dependent material and tracking material interface. A common practice  
37 in modeling HE explosion problems is to discretize the structure by Lagrangian  
38 finite elements and then the explosion effects are taken into account by applying  
39 the pressure load on the structure surface. For examples, a plate under air blast  
40 loading was studied by Jacinto et al. [Jacinto, Ambrosini, and Danesi (2001)] and  
41 the spallation in reinforced concrete plates subjected to blast loading was studied  
42 by Xu et al. [Xu and Lu (2006)]. However, the Lagrangian finite element method  
43 (FEM) suffers from mesh tangling which deteriorates its numerical accuracy and  
44 efficiency dramatically.

45 Recently, many meshless methods based on Lagrangian framework have been pro-  
46 posed as the alternatives for the traditional finite element methods, which have  
47 showed advantages for problems associated with large deformation. Among them,  
48 the smoothed particle hydrodynamics (SPH) [Lucy (1977); Liu and Liu (2003)] and  
49 material point method (MPM) [Sulsky, Chen, and Schreyer (1994); Sulsky, Zhou,  
50 and Schreyer (1995)] have been successfully applied to HE explosion problems.  
51 Detonations of HE in air and underwater were simulated by SPH [Liu, Liu, Zong,  
52 and Lam (2003); Liu, Liu, Lam, and Zong (2003b)]. The numerical tests revealed  
53 the ability of SPH in modeling explosion problems with arbitrary charge shape and  
54 different orientations. Ma et al. [Ma, Zhang, Lian, and Zhou (2009)] proposed an  
55 adaptive MPM for simulating the HE explosion problems whilst Lian et al. [Lian,  
56 Zhang, Zhou, Ma, and Zhao (2011)] extended the MPM method to the explosively  
57 driven metal problems whose numerical results agreed well with the Gurney solu-  
58 tions. Zhang et al. [Zhang, Zou, VanderHeyden, and Ma (2008); Zhang, Ma, and  
59 Giguere (2011)] enhanced MPM to simulate a series of fluid-structure interactions  
60 and multi-material interactions problems. Using MPM, Banerjee [Banerjee (2004)]  
61 simulated the fragmentation of cylinders due to explosively expanding gases gener-  
62 ated by a high energy material inside the cylinders, and Hu et al. [Hu and Chen  
63 (2006)] studied the synergistic effects of blast and fragmentation on a concrete wall.  
64 Furthermore, a comparison study of MPM and SPH in modeling hyper velocity im-  
65 pact problems was conducted by Ma et al. [Ma, Zhang, and Qiu (2009)]. These

66 studies concluded that these two methods possesses a great potential for simulating  
67 large deformation FSI problems at high strain-rate. However, the particle methods  
68 require more computational resource and have difficulties to construct high order  
69 scheme when simulating the fluid in high explosive (HE) explosion problems.

70 In contrast to the Lagrangian method, the Eulerian method employes fixed meshes  
71 so it is not plagued by mesh distortion. They usually solve the fluid region in HE  
72 explosion problem together with approaches for tracking the material interfaces and  
73 the internal history variables, such as the Youngs interface reconstruction method  
74 [Youngs (1982)], level set method [Osher and Fedkiw (2001)] and fuzzy interface  
75 method [Ning and Chen (2004)]. Ma et al. [Ma, Wang, and Ning (2008)] developed  
76 a multi-material Eulerian hydrodynamic code with modified Youngs' interface re-  
77 construction algorithm for the simulations of explosion problems such as explosion  
78 in tunnel and steel shaped charge jet. Luccioni et al.[Luccioni, Ambrosini, and  
79 Danesi (2004)] employed AUTODYN to study the structural failure of a reinforced  
80 concrete building inflicted by an air blast load. The dispersion process of the HE  
81 products in air was simulated by the three-dimensional Euler FCT solver. Wu et  
82 al. [Wu and Hao (2005)] simulated the ground shock and air blast pressure gener-  
83 ated from surface explosions using AUTODYN2D. Furthermore, newly developed  
84 methods based on Eulerian framework such as Discontinuous Galerkin Method  
85 (DGM) [Cockburn, Hou, and Shu (1990)] has been used to solve the gaseous deto-  
86 nation problems [Wang, Zhang, Shu, and Ning (2012)]. These studies show sound  
87 ability of Eulerian method in solving wave propagation process in HE explosion  
88 problems. However, the Eulerian description limits its ability to handle the FSI  
89 problems by one single method, so it is usually coupled with a Lagrangian method  
90 to discretize the region of structures.

91 There are also some mixed methods which take the advantages of both Lagrangian  
92 and Eulerian descriptions. A well-known example is the arbitrary Lagrangian-  
93 Eulerian method (ALE) [Liu, Belytschko, and Chang (1986)]. The major numerical  
94 difficulty of ALE is developing an effective and efficient mesh moving scheme for  
95 complicated 3D problems. Furthermore, the numerical diffusion and dissipation  
96 still exist in ALE method. A detailed review on Lagrangian, Eulerian and their  
97 mixed methods was presented by Benson [Benson (1992)].

98 Since the Lagrangian method possess advantages in simulating the structures with  
99 historical variables and the Eulerian method handle the fluid better, much effort  
100 has been devoted to couple these two type of methods so as to take advantage of  
101 each method to simulate the HE explosion and the relevant large deformation prob-  
102 lems. Fairlie et al. [Fairlie and Bergeron (2002)] described a coupled methodology  
103 for simulating the surface-laid or buried charges explosions. In the methodology,  
104 the air and explosive were modeled in an Euler-FCT grid as a single ideal gas

105 while the surrounding soil and complex targets were modeled by Lagrangian grid.  
106 Zhang et al. [Zhang and Xu (2007)] investigated a cylindrical shell loaded by blast  
107 wave from a central charge. Finite volume method (FVM) was used to model the  
108 HE in ALE framework and FEM was adopted to model the shell in Lagrangian  
109 framework. Guillkey et al. [Guilkey, Harman, and Banerjee (2007)] developed  
110 an approach for solving full-physics FSI problems using the Eulerian description  
111 (FVM) for fluids and the Lagrangian description (MPM) for solids. To simulate  
112 FSI problems with large deformations in the structure, Gilmanov et al. [Gilmanov  
113 and Acharya (2008)] developed an effective numerical method in which the hybrid  
114 immersed boundary method (HIBM) was employed to resolve complex boundaries  
115 for the fluid flow and MPM was coupled to resolve the structural stresses and de-  
116 formation. The combined method was implemented in the framework of finite  
117 difference method (FDM). Flekkoy et al. [Flekkoy, Wagner, and Feder (2000)] in-  
118 troduced a “hybrid model” that permits a continuum description in one region to be  
119 coupled to an atomistic description in another region. The two regions were solved  
120 by FDM and molecular dynamics (MD) respectively.

121 Coupling between meshless methods and FEM are also carried out to simulate the  
122 problems with large deformation. Aktay et al. [Aktay and Johnson (2007)] devel-  
123 oped a FEM/SPH coupling technique for high velocity impact (HVI) simulation of  
124 composite panels. In the technique, contact interfaces were employed to couple the  
125 discrete smoothed particles and finite elements which were employed to model the  
126 parts undergoing large and small deformation, respectively. Zhang et al. [Zhang,  
127 Sze, and Ma (2006)] developed an explicit material point finite element method  
128 for HVI. In their method, the momentum equations were solved on a predefined  
129 regular grid in the severely deformed region and on FE mesh elsewhere. Lian et  
130 al. [Lian, Zhang, Zhou, and Ma (2011)] developed a coupled approach in which  
131 the bodies with large and mild deformation were discretized by MPM and FEM,  
132 respectively. The interaction between two bodies was handled by a contact method  
133 and the FE nodes on the contact interface were treated as special particles. To fur-  
134 ther improve the efficiency, Lian et al. [Lian, Zhang, and Liu (2012)] proposed an  
135 adaptive material point finite element method in which material domains were ini-  
136 tially discretized into finite elements (FE). Depending on severity of the distortion  
137 or plastic strain being developed, some elements were adaptively converted into  
138 MPM particles during the solution process.

139 Most of the coupling between Lagrangian methods and Euler methods divide the  
140 computational domain by an interface between fluid and structure in solving FSI  
141 problems. Individual materials occupy distinct regions in space, with interactions  
142 occurring at the material interfaces. Because of the separated nature of the materi-  
143 als, the interface requires additional treatment and often introduce numerical error.

144 In this paper, a coupled finite difference material point (CFDMP) method is de-  
145 veloped to model the 3D HE explosion and its interaction with the surrounding  
146 structures. Taking the advantage of handling the shock wave propagation, FDM  
147 is employed to simulate a large proportion of the fluid region, while MPM is em-  
148 ployed in the FSI region which contains the structures and the fluid near the struc-  
149 tures. Therefore, the interface between two computational regions is located in the  
150 same material region (fluid) and the interface effect could be significantly reduced.  
151 The material interface is located in the MPM region so that the fluid-structure in-  
152 teraction is solved in MPM region to fully take its sound ability for simulating  
153 history-dependent material and tracking the material interface. Hence, the region  
154 involved shock wave dispersion problem is simulated by FDM and the region in-  
155 volved history-dependent materials and FSI problems are simulated by MPM. The  
156 interaction between FDM region and MPM region are implemented by a “bridge  
157 region” which contains only one material. MPM provides the boundary condition  
158 for FDM region by mapping the value from background grid nodes to the fictitious  
159 points outside the boundary of FDM, while FDM provides the boundary condi-  
160 tion for MPM region by mapping value from cell-centre points to MPM interface  
161 grid nodes. The transportation between the two computational regions is imple-  
162 mented by moving particles in the bridge region. The proposed scheme has been  
163 implemented in our 3D explicit material point method code, MPM3D, to simulate  
164 HE explosion problems. Several numerical examples are presented to validate the  
165 efficiency and accuracy of the proposed method.

166 The remaining part of this paper is organized as follows. Section 2 presents the  
167 governing equations and the numerical scheme in each computational region. A  
168 description of CFDMP and the numerical implementations are presented in Sec-  
169 tion 3. Then the material models employed are introduced in Section 4. Several  
170 numerical tests are given in Section 5, and the conclusions are summarized in Sec-  
171 tion 6.

## 172 **2 Governing equations and schemes**

173 The problem domain can be divided into two computational regions in space. FDM  
174 is employed to simulate the fluid region, while the FSI region is simulated by MPM.  
175 Since the primary materials and their properties are different in two regions, differ-  
176 ent governing equations and schemes are employed as follows.

### 177 **2.1 Governing equations and scheme in FDM region**

The dispersion process of detonation products to the surrounding air is a flow with strong discontinuity. Owing to the extremely high detonation and dispersion speeds, the explosion process is adiabatic. The detonation products and the

surrounding air can be assumed to be inviscid and compressible, which can be described by the three-dimensional compressible Euler equations

$$\frac{\partial U}{\partial t} + \frac{\partial f(U)}{\partial x} + \frac{\partial g(U)}{\partial y} + \frac{\partial h(U)}{\partial z} = 0 \quad t \geq 0, (x, y, z) \in \mathbb{R}^3 \quad (1)$$

with suitable equation of state (EOS). In Eq. (1),

$$\begin{cases} U = [\rho, \rho \dot{u}_1, \rho \dot{u}_2, \rho \dot{u}_3, E]^T \\ f(U) = [\rho \dot{u}_1, \rho \dot{u}_1^2 + p, \rho \dot{u}_1 \dot{u}_2, \rho \dot{u}_1 \dot{u}_3, (E + p) \dot{u}_1]^T \\ g(U) = [\rho \dot{u}_2, \rho \dot{u}_1 \dot{u}_2, \rho \dot{u}_2^2 + p, \rho \dot{u}_2 \dot{u}_3, (E + p) \dot{u}_2]^T \\ h(U) = [\rho \dot{u}_3, \rho \dot{u}_1 \dot{u}_3, \rho \dot{u}_2 \dot{u}_3, \rho \dot{u}_3^2 + p, (E + p) \dot{u}_3]^T \end{cases} \quad (2)$$

178 where  $\dot{u}_1$ ,  $\dot{u}_2$  and  $\dot{u}_3$  are the velocity components along the x-, y- and z- directions,  
179 respectively;  $E = \frac{1}{2}\rho(\dot{u}_1^2 + \dot{u}_2^2 + \dot{u}_3^2) + \rho e$  is the total energy per unit volume;  $e$  is the  
180 specific internal energy and pressure  $p$  can be obtained from an EOS.

The explicit three-dimensional scheme of fractional step FDM is outlined in a time step (from  $n$  to  $n + 1$ ) as below [Yanenko (1971)]. Take  $x$  direction as an example, adaptive artificial viscosity [Zhang (2010)] is used to avoid the non-physical oscillations near the shockwave which can be written as

$$\bar{U}_i^n = U_i^n + \frac{1}{2}\eta\theta_i^n(U_{i+1}^n - 2U_i^n + U_{i-1}^n) \quad (3)$$

$$\theta_i^n = \frac{\left| \rho_{i+1}^n - \rho_i^n \right| - \left| \rho_i^n - \rho_{i-1}^n \right|}{\left| \rho_{i+1}^n - \rho_i^n \right| + \left| \rho_i^n - \rho_{i-1}^n \right|} \quad (4)$$

where  $\eta$  is a parameter to be adjusted empirically to meet the requirements for different problems or determined according to the time step  $\Delta t$ , spatial step  $\Delta x$  and sound speed  $c$  as

$$\eta = \frac{c\Delta t}{\Delta x} \left(1 - \frac{c\Delta t}{\Delta x}\right) \quad (5)$$

The fractional steps method [Yanenko (1971)] is introduced to split the three-dimensional problem into three one-dimensional flow problems. To reduce the artificial affect introduced by the integration sequence, the splitting can be implemented as

$$U^{n+1} = L_z\left(\frac{1}{2}\Delta t\right)L_y\left(\frac{1}{2}\Delta t\right)L_x\left(\frac{1}{2}\Delta t\right)L_x\left(\frac{1}{2}\Delta t\right)L_y\left(\frac{1}{2}\Delta t\right)L_z\left(\frac{1}{2}\Delta t\right)U^n \quad (6)$$

where  $L_x\left(\frac{1}{2}\Delta t\right)$  is the difference operator in x direction of Eq. (1),  $L_y\left(\frac{1}{2}\Delta t\right)$  is the difference operator in y direction of Eq. (1) and  $L_z\left(\frac{1}{2}\Delta t\right)$  is the difference operator

in z direction of Eq. (1),  $U^n$  are the conservation variables  $\bar{U}_i^n$  defined in Eq.(3). In this paper, a second order Lax-Wendroff [Lax and Wendroff (1964)] finite difference scheme is employed for each direction so that

$$L_x(\Delta t)U_i^n = U_i^n - \frac{1}{2} \frac{\Delta t}{\Delta x} [f(U_{i+1}^n) - f(U_{i-1}^n)] + \frac{1}{2} \left(\frac{\Delta t}{\Delta x}\right)^2 [f(U_{i+1}^n) - 2f(U_i^n) + f(U_{i-1}^n)] \quad (7)$$

$$L_y(\Delta t)U_j^n = U_j^n - \frac{1}{2} \frac{\Delta t}{\Delta y} [g(U_{j+1}^n) - g(U_{j-1}^n)] + \frac{1}{2} \left(\frac{\Delta t}{\Delta y}\right)^2 [g(U_{j+1}^n) - 2g(U_j^n) + g(U_{j-1}^n)] \quad (8)$$

$$L_z(\Delta t)U_k^n = U_k^n - \frac{1}{2} \frac{\Delta t}{\Delta z} [h(U_{k+1}^n) - h(U_{k-1}^n)] + \frac{1}{2} \left(\frac{\Delta t}{\Delta z}\right)^2 [h(U_{k+1}^n) - 2h(U_k^n) + h(U_{k-1}^n)] \quad (9)$$

## 181 2.2 Governing equations and scheme in MPM region

During fluid-structure interaction, the history variables are important to describe the behavior of the structure. Therefore, the updated Lagrangian description is employed for the continuum which is governed by the momentum equation

$$\sigma_{ij,j} + \rho f_i = \rho \ddot{u}_i \quad \forall x_i \in V \quad (10)$$

where  $V$  is the current material domain,  $\sigma_{ij}$  is the Cauchy stress,  $\rho$  is the current density,  $f_i$  is the body force density,  $\ddot{u}_i$  is the acceleration. The weak form of governing equation (10) can be obtained from the weighted residual method as [Sulsky, Chen, and Schreyer (1994)]

$$\delta \Pi = \int_V \rho \ddot{u}_i \delta u_i dV + \int_V \sigma_{ij} \delta u_{i,j} dV - \int_V \rho f_i \delta u_i dV - \int_{A_t} \bar{t}_i \delta u_i d\Gamma = 0 \quad (11)$$

182 where  $A_t$  is the portion of boundary prescribed with traction  $\bar{t}_i$ .

The mass conservation equation is

$$\rho J = \rho_0 \quad (12)$$

where  $J$  is the determinant of the deformation gradient matrix  $F_{ij} = \partial x_i / \partial X_j$  and  $\rho_0$  is the initial density. The energy equation is given by

$$\dot{E} = J \sigma_{ij} \dot{\epsilon}_{ij} = J s_{ij} \dot{\epsilon}_{ij} - J p \dot{\epsilon}_{kk} \quad (13)$$

183 where  $E$  is the energy per unit initial volume,  $\dot{\epsilon}_{ij}$  is the strain rate,  $s_{ij} = \sigma_{ij} - p\delta_{ij}$   
 184 is the deviatoric stress and  $p$  represents the pressure.

185 In CFDMP method, these governing equations will be solved by MPM as described  
 186 in existing literature [Ma, Hanan, Komanduri, and Lu (2012)]. MPM is an ex-  
 187 tension of the FLIP particle in cell (PIC) method [Brackbill and Ruppel (1986)]  
 188 in computational fluid dynamics to computational solid mechanics. As a pre-  
 189 processing step, we define the background grid in the FSI region, and discretize  
 190 the material region by a set of particles, see Fig.1. All the material variables in-  
 191 cluding mass, position, velocity, strain and stress are carried by the particles. In  
 192 each time step, the particles are rigidly attached to the background grid in which  
 193 the momentum equation is solved in the framework of the standard finite element  
 194 method. Then, the positions and velocities of all particles are updated based on the  
 195 grid nodal velocities and accelerations. Afterward, the deformed grid is discarded  
 196 and a new regular grid is used in next time step, and the initial grid nodal mass and  
 197 momentum can be obtained from the mass and momentum of particles. Thus, com-  
 198 plications associated with mesh distortion are avoided. In general, a fixed regular  
 199 grid can be used throughout the computation.

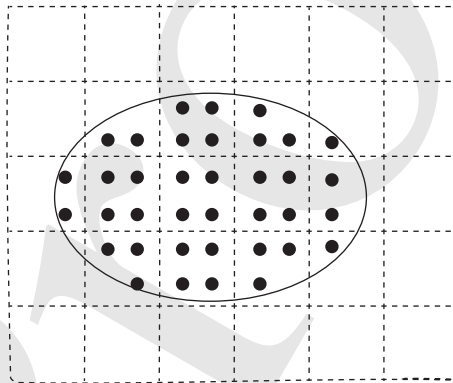


Figure 1: Material point discretization

Since the material domain is discretized with a set of particles, the density can be approximated as

$$\rho(x) = \sum_{p=1}^{n_p} m_p \delta(x - x_p) \quad (14)$$

200 where  $n_p$  denotes the number of particles;  $\delta$  is the Dirac Delta function;  $m_p$  is  
 201 the mass and  $x_p$  is the position of particle  $p$ . Since the masses are carried by the  
 202 particles, the mass conservation is automatically satisfied in MPM.

Since the particles are rigidly attached to the computational grid, the displacement of particle  $p$  can be obtained by mapping from their grid node values  $u_I$  using the standard finite element interpolation functions of the grid as

$$u_p = \sum_{I=1}^{n_g} N_{Ip} u_I \quad (15)$$

where  $N_{Ip} = N_I(x_p)$  is the interpolation function of grid node  $I$  evaluated at the position of particle  $p$ . The 8-node hexahedron interpolation is used whose shape function is given by

$$N_{Ip} = \frac{1}{8}(1 + \xi_p \xi_I)(1 + \eta_p \eta_I)(1 + \zeta_p \zeta_I) \quad I = 1, 2, \dots, 8 \quad (16)$$

203 where  $(\xi_I, \eta_I, \zeta_I)$  take their nodal value of  $\pm 1$  on grid node  $I$ , and  $(\xi_p, \eta_p, \zeta_p)$  de-  
 204 note the natural coordinates of particle  $p$ . If the particle  $p$  is outside the hexahedron,  
 205  $N_{Ip} = 0$ .

Substituting (14) and (15) into the weak form (11) and using a lumped mass matrix lead to

$$\dot{p}_{il} = f_{il}^{\text{int}} + f_{il}^{\text{ext}} \quad (17)$$

where

$$p_{il} = \sum_{p=1}^{n_p} m_p N_{Ip} v_{ip} \quad (18)$$

is the grid nodal momentum,

$$f_{il}^{\text{int}} = - \sum_{p=1}^{n_p} N_{Ip,j} \sigma_{ijp} \frac{m_p}{\rho_p} \quad (19)$$

is the grid nodal internal force and

$$f_{il}^{\text{ext}} = \sum_{p=1}^{n_p} m_p N_{Ip} f_{ip} + \sum_{p=1}^{n_p} N_{Ip} h^{-1} t_{ip} \frac{m_p}{\rho_p} \quad (20)$$

is the grid nodal external force. In Eq.(20),  $h$  denotes the thickness of the boundary layer used to calculate the surface integral. The grid nodal masses can be obtained by

$$m_I = \sum_{p=1}^{n_p} N_{Ip} m_p \quad (21)$$

From time step  $n$  to  $n + 1$ , the momentum equation is integrated by

$$p_{il}^{n+1} = p_{il}^n + f_{il}^n \Delta t^n \quad (22)$$

where

$$f_{il}^n = f_{il}^{\text{int},n} + f_{il}^{\text{ext},n} \quad (23)$$

The velocity and position of particles are updated by mapping the increments from background grid nodes back to particles as

$$v_{ip}^{n+1} = v_{ip}^n + \sum_{l=1}^8 \frac{f_{il}^n}{m_l^n} N_{lp}^n \Delta t^n \quad (24)$$

$$x_{ip}^{n+1} = x_{ip}^n + \sum_{l=1}^8 \frac{p_{il}^n}{m_l^n} N_{lp}^n \Delta t^n \quad (25)$$

Before calculating the incremental strain and spin tensors, the updated velocities of the particles are mapped back to the grid nodes to update their velocities, namely

$$v_{il}^{n+1} = \frac{\sum_{p=1}^{n_p} m_p N_{lp}^n v_{ip}^{n+1}}{m_l^n} \quad (26)$$

The incremental strain and spin tensors are calculated by (take three-dimensional problems for example)

$$\Delta \epsilon_{ijp}^n = \frac{1}{2} \sum_{l=1}^8 (N_{lp,j}^n v_{il}^{n+1} + N_{lp,i}^n v_{jl}^{n+1}) \Delta t^n \quad (27)$$

$$\Delta \Omega_{ijp}^n = \frac{1}{2} \sum_{l=1}^8 (N_{lp,j}^n v_{il}^{n+1} - N_{lp,i}^n v_{jl}^{n+1}) \Delta t^n \quad (28)$$

Finally, the density and stress of particles are updated by

$$\rho_p^{n+1} = \rho_p^n / (1 + \Delta \epsilon_{kkp}^n) \quad (29)$$

$$\sigma_{ijp}^{n+1} = \sigma_{ijp}^n + \sigma_{ikp}^n \Delta \Omega_{jkp}^n + \sigma_{jkp}^n \Delta \Omega_{ikp}^n + \Delta \sigma_{ijp}^n \quad (30)$$

206 where  $\Delta \sigma_{ijp}^n$  is calculated by a material constitutive model introduced in Section 4.  
 207 After all the history information has been updated and stored in particles, time step  
 208  $n$  ends up and the deformed background grid is discarded. Time step  $n + 1$  starts  
 209 with a new regular grid being employed.

### 210 3 Coupled finite difference material point method

211 Fig. 2 shows a typical HE air explosion problem. A HE charge is burned into  
 212 gaseous products which disperse to the surrounding air and then interact with the  
 213 structure. The whole region can be divided into a fluid region and a FSI region  
 214 separated by the dash line. The traditional FDM is employed to simulate the dis-  
 215 persion process in fluid region. When the pressure of cell-centres near the region  
 216 interface, i.e. the dash line in Fig. 2, attains a prescribed threshold, arrival of the  
 217 shock wave front is detected and the interaction region will be activated. The inter-  
 218 action process is simulated by MPM so that the history variables of structure can  
 219 be recorded to characterize the material damage. The detailed governing equations  
 220 and schemes for the two regions have been presented in Section 2. The interaction  
 221 between FDM region and MPM region is provided as follow.

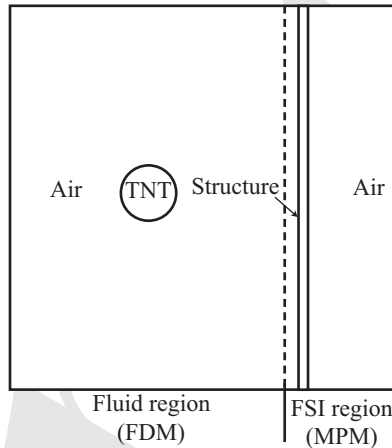


Figure 2: A typical HE explosion problem

#### 222 3.1 Bridge region

223 As shown in Fig. 3, the whole problem domain is discretized to  $m$  regular cells in  
 224  $x$  direction ( $y, z$  directions are also applicable). The size of FDM cells and MPM  
 225 background cells are the same. The cells from 0 to  $k$  are FDM cells and the cells  
 226 from  $k - w$  to  $m$  are MPM background cells, where  $w$  denotes the number of cells  
 227 in the bridge region in direction  $x$ . Cells from  $k - w$  to  $k$  define the bridge region,  
 228 in which the FDM cells are coincident with the MPM background cells. As shown  
 229 in Fig. 3, two different materials in the MPM region are marked by circles and  
 230 triangles respectively. The material in the FDM region is the same as the fluid

231 material in the MPM region, air is taken for example here, and the structures in the  
 232 MPM region could have complex geometry because it is discretized by particles.  
 233 The variables of fictitious points (hollow squares) outside the FDM region in cell  
 234  $k + 1$  is obtained by interpolating the background grid nodes while the variables of  
 235 interface nodes (hollow circles) of the MPM region is adjusted by interpolating the  
 236 centers of cell  $k - w - 1$  after being initialized by Eqs. (18) to (21). The transport  
 237 between the two computational regions is implemented by moving the particles  
 238 through the cell interface between the cells  $k - w - 1$  and  $k - w$ . The detailed  
 239 methods and equations will be described in the following subsections.

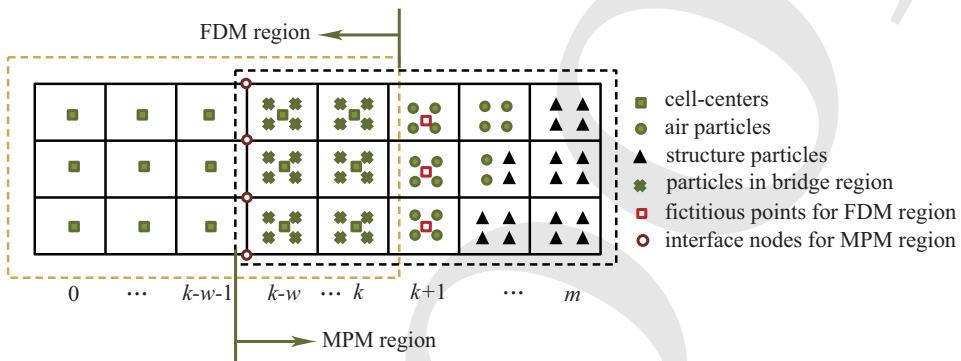


Figure 3: The computational region for CFDMP

240 **3.2 Interface boundary condition for FDM region**

To solve Eq. (1) in FDM region, the variables of fictitious points ( $k + 1$ ) outside FDM region as shown in Fig. 3 should be given. The mass  $m_c^n$  and momentum  $p_{ic}^n$  of the FDM's fictitious points in time step  $n$  can be obtained by mapping the MPM grid nodal mass and momentum via the shape function, namely (take three-dimensional problems for example)

$$m_c^n = \sum_{l=1}^8 m_l^n N_{lc}^n \tag{31}$$

$$p_{ic}^n = \sum_{l=1}^8 p_{il}^n N_{lc}^n \tag{32}$$

The internal energy  $e_c^{\text{int},n}$  is calculated by adding all the particles' internal energy in

the cell as

$$e_c^{\text{int},n} = \sum_{p=1}^{n_p} e_p^{\text{int},n} \quad (33)$$

Finally, the variables of the cell-centre  $k+1$  for FDM can be obtained by

$$\rho_c^n = \frac{m_c^n}{V_c} \quad (34)$$

$$(\rho v)_{ic}^n = \rho_c^n \frac{p_{ic}^n}{m_c^n} \quad (35)$$

$$E_c^n = \frac{e_c^{\text{int},n} + \frac{1}{2} m_c^n \left( \frac{p_{ic}^n}{m_c^n} \right)^2}{V_c} \quad (36)$$

### 241 3.3 Interface boundary condition for MPM region

To solve the governing equations in MPM region, the variables of grid interface nodes between cell  $k-w-1$  and cell  $k-w$  of MPM region (see Fig. 3) should be adjusted to consider the effect from the FDM region. The FDM cell-centers with cell number  $k-w-1$  in direction  $x$  are considered as particles and take part in the mapping process from particles to background nodes as in Eqs. (18), (19) and (21). Therefore, the mass, momentum and internal force of the background grid interface nodes of MPM are adjusted by

$$m_I^n = \sum_{p=1}^{n_p} N_{Ip}^n m_p + \sum_{c=1}^{n_c} \rho_c^n N_{Ic}^n V_c^n \quad (37)$$

$$p_{il}^n = \sum_{p=1}^{n_p} m_p N_{Ip}^n v_{ip}^n + \sum_{c=1}^{n_c} \rho_c^n V_c^n v_{ic}^n N_{Ic}^n \quad (38)$$

$$f_{il}^{\text{int},n} = - \sum_{p=1}^{n_p} N_{Ip,j}^n \sigma_{ijp} \frac{m_p}{\rho_p} + \sum_{c=1}^{n_c} N_{Ic,i}^n p_c^n V_c^n \quad (39)$$

242 where the first term is the same as those in Eqs. (18), (19) and (21) in the standard  
 243 MPM, while the second term is the contribution from the FDM region. The sub-  
 244 script “ $c$ ” denotes the cells in the FDM region which are connected to the MPM  
 245 interface node being adjusted,  $n_c$  is the number of the cells, and  $p_c^n$  denotes the  
 246 pressure.

247 **3.4 Transportation between FDM and MPM regions**

248 After integrating the governing equations in FDM region, the variables have been  
 249 updated for every cell, and the transportation between the two computational re-  
 250 gions is carried out by moving the particles through the boundary of the MPM  
 251 region. We take a pair of the interface cells as an example as shown in Fig. 4. Both  
 252 two cells are in the FDM region and the right cell, which is a bridge cell, is also  
 253 in the MPM region. The interface between these two cells are the boundary of the  
 254 MPM region.

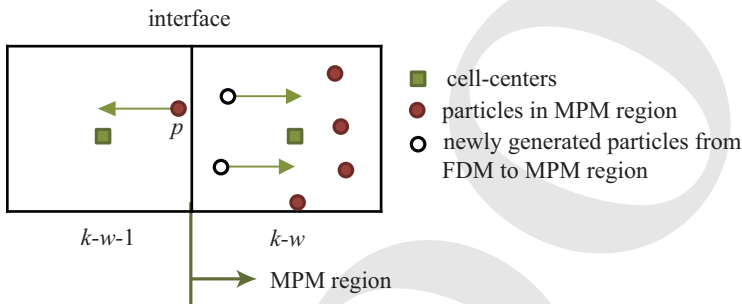


Figure 4: The transportation between FDM and MPM

Assume that the time step  $n$  has been solved and the transportation is needed. We first get the density, velocity and pressure of the interface by interpolating the cell-center values of these two cells

$$\rho_f^n = \frac{1}{2}(\rho_{k-w-1}^n + \rho_{k-w}^n) \tag{40}$$

$$v_{if}^n = \frac{1}{2}(v_{k-w-1}^n + v_{k-w}^n), \quad i = 1, 2, 3 \tag{41}$$

$$p_f^n = \frac{1}{2}(p_{k-w-1}^n + p_{k-w}^n) \tag{42}$$

The fluxes of mass and momentum transferred during this time step can be calculated as

$$f_m^n = \rho_f^n v_{1f}^n \Delta y \Delta z \Delta t^n \tag{43}$$

$$f_{ip}^n = \rho_f^n v_{if}^n v_{1f}^n \Delta y \Delta z \Delta t^n, \quad i = 1, 2, 3 \tag{44}$$

255 where  $v_{1f}^n$  is the normal velocity of the interface determined by Eq.(41).

Referring to the work by Flekkoy [Flekkoy, Wagner, and Feder (2000)] on coupling FDM and molecular dynamics(MD), particles are generated in cell  $k - w$  to guarantee the conservation of mass and momentum. The newly generated particles have the same density, velocities and pressure as they are in the “donor cell”. To make sure the newly generated particles do not have extreme distinction with existing particles in mass to improve the stability, we determine their number and mass by

$$s = \text{ceiling}\left(\frac{f_m^n}{m_e^n}\right) \quad (45)$$

$$m_p = \frac{f_m^n}{s} \quad (46)$$

where  $m_e^n$  is the mass of the existing particles. We slightly adjust  $s$  to an integer multiple of 4 to distribute particles uniformly. The furthest particles’ distance from the center of the interface are calculated by their velocity in this step as

$$d_i = v_i^n \Delta t^n, \quad i = 1, 2, 3 \quad (47)$$

Moreover, the internal energy of the newly generated particles are given by their EOS as (air taking for example)

$$e_p^{\text{int},n} = \frac{p_p^n m_p^n}{(\gamma - 1)\rho_p^n} \quad (48)$$

256 where  $p_p^n$  is the pressure of the newly generated particles. Since the equation is  
 257 linear about mass, the conservation of internal energy is protected here. The newly  
 258 generated particles in same cells have single velocity, and the mass conservation  
 259 is automatically protected, so kinetic energy flow into the MPM region is equal to  
 260 that carried by the newly generated particles. Together, the energy conservation is  
 261 protected in this process.

If the particles in cell  $k - w$  cross the boundary of MPM region in this step, the transportation is from MPM to FDM. The crossing particles will not take part in the computation of MPM any more, and their conservation variables are added to the cell they move into. So the conservation is also protected in this process. For example, the particle  $p$  moves from cell  $k - w$  into cell  $k - w - 1$  in Fig. 4, so the cell-center values of cell  $k - w - 1$  should be adjusted by

$$\rho_c^{n'} = \frac{\rho_c^n \Delta x \Delta y \Delta z + m_p^n}{\Delta x \Delta y \Delta z} \quad (49)$$

$$\rho u_{ic}^{n'} = \frac{\rho_c^n u_{ic}^n \Delta x \Delta y \Delta z + m_p^n u_{ip}^n}{\Delta x \Delta y \Delta z} \quad (50)$$

$$E_c^{n'} = \frac{E_c^n \Delta x \Delta y \Delta z + e_p^n}{\Delta x \Delta y \Delta z} \quad (51)$$

### 262 3.5 Numerical implementation

263 One explicit step using CFDMP (from  $n$  to  $n + 1$ ) is summarized below.

264 (1) Calculate the time step for MPM and FDM by CFL criterion respectively, and  
265 take the smallest one as the time step for CFDMP.

266 (2) Map the mass  $m$  and momentum  $p$  of all MPM particles to the background grid  
267 except the interface nodes by Eqs. (21) and (18).

268 (3) Map the mass  $m$  and momentum  $p$  of corresponding MPM particles to the  
269 interface nodes of background grid by Eqs. (37) and (38).

270 (4) Compute the grid nodal internal force  $f^{\text{int}}$  and external force  $f^{\text{ext}}$  except the  
271 interface nodes by Eqs. (19) and (20).

272 (5) Compute the grid nodal internal force  $f^{\text{int}}$  of interface nodes by Eq. (39).

273 (6) Integrate the momentum equation by Eq. (22).

274 (7) Update the fictitious points' variables by Eqs. (34) to (36).

275 (8) Integrate the governing equations of FDM by Eq. (6), where the operators in  
276 three directions are defined by Eqs. (7) to (9).

277 (9) Update the velocity and position of particles by mapping their increments back  
278 to particles by Eqs. (24) and (25).

279 (10) Map the velocity back to the grid nodes by Eq. (26).

280 (11) Calculate the incremental strain and spin tensors by Eqs. (27) and (28).

281 (12) Update the density of particles by Eq. (29).

282 (13) Update the stress of particles  $\sigma_{ijp}^{n+1}$  by Eq. (30).

283 (14) Carry out the transportation process between FDM region and MPM region as  
284 described in Section 3.4 and this completes the current time step .

## 285 4 Material models

286 Equations of state, constitutive models and reaction models complete the whole  
287 governing equations. Brief descriptions of the models used in this paper are given  
288 below. Some of the parameters are taken from the references as well as the com-  
289 mercial software such as AUTODYN and LS-DYNA.

### 290 4.1 High explosive EOS

291 In detonation process, the reactive wave propagates at very high speed inside the  
292 HE [Zukas and Walters (1998)]. The exothermic reaction is completed within a  
293 few microseconds with the HE completely converted to gaseous products. Most of  
294 the earlier works use the "artificial detonation model" [Liu and Liu (2003)] which

295 considers the explosive as a group of gaseous products with the same energy and  
 296 volume of the initial explosive charge. For most simulations in this paper, we use  
 297 the “real detonation model” [Liu and Liu (2003)] which lights the explosive ac-  
 298 cording to the reactive wave’s propagation, the pressure jump which occurs when  
 299 the shock front arrived at material interface is better captured [Cui, Zhang, Sze, and  
 300 Zhou (2013)]. For saving computational resources and accelerating the simulation,  
 301 we refer to the remap method in AUTODYN for air explosion problem, solving an  
 302 1D TNT explosion problem first and map the result to the 3D region as the initial  
 303 condition in FDM region. Finer grid can be allocated for the 1D simulation, which  
 304 is in favour of describing the strong discontinuity during the detonation process and  
 305 the initial stage of the dispersion process.

We simulate the 1D TNT explosion by MPM so as to conveniently model the det-  
 onation process by “real detonation model”. In the initialization phase, a lighting  
 time  $t_L$  is calculated for each particle (MPM) by dividing the distance from the det-  
 onation point by the detonation speed. After the detonation, the gaseous products  
 are controlled by the EOS. The real pressure  $p$  of the gaseous products is deter-  
 mined by multiplying the pressure  $p_E$  obtained from EOS with a burn fraction  $F$   
 that controls the release of chemical energy [Hallquist (1998)], namely

$$p = F \cdot p_E \quad (52)$$

$$F = \begin{cases} \frac{(t-t_L)D}{1.5h} & t > t_L \\ 0 & t < t_L \end{cases} \quad (53)$$

306 where  $h$  is the characteristic size of a particle and  $t$  denotes the current time. Several  
 307 time steps are often required for  $F$  to reach unity. Once it is done,  $F$  is kept at unity.  
 308 Using this method, the discontinuous detonation wave is smoothed and assumes a  
 309 continuous but rapidly changing wavefront.

After detonation, the gaseous products are described by Jones-Wilkins-Lee(JWL)  
 EOS

$$p = A\left(1 - \frac{\omega}{R_1 V}\right)e^{-R_1 V} + B\left(1 - \frac{\omega}{R_2 V}\right)e^{-R_2 V} + \frac{\omega E_0}{V} \quad (54)$$

310 Moreover, TNT with a density of  $1630\text{kg/m}^3$  and a detonation speed of  $6930\text{m/s}$   
 311 are used in the simulation. The parameters of JWL EOS are taken from [Liu, Liu,  
 312 Lam, and Zong (2003a)] as  $A = 3.712 \times 10^{11}\text{N/m}^2$ ,  $B = 3.21 \times 10^9\text{N/m}^2$ ,  $R_1 =$   
 313  $4.15$ ,  $R_2 = 0.95$ ,  $\omega = 0.3$ , energy per initial volume  $E_0 = 6993 \times 10^6\text{J/m}^3$ .

314 **4.2 Air model**

Air is modeled as a null material model with the following ideal gas EOS

$$p = (\gamma - 1)\rho e = (\gamma - 1)\left[E - \frac{1}{2}\rho(u_1^2 + u_2^2 + u_3^2)\right] \quad (55)$$

315 where  $\rho = 1.225 \text{ kg/m}^3$  and  $e = 2.0685 \times 10^5 \text{ J/kg}$ .

316 **4.3 Concrete model with tensile damage**

The concrete is modeled by Holmquist Johnson Cook (HJC) model with tensile damage. The HJC model was originally presented for concrete damage problems involving hydrostatic pressure, strain rate and compressive damage. The equivalent strength is expressed as

$$\sigma^* = [A(1 - D) + Bp^{*N}][1 + C \ln \dot{\epsilon}^*] \quad (56)$$

where  $\sigma^* = \sigma/f'_c$  denotes the normalized equivalent stress,  $\sigma$  is the actual equivalent stress,  $f'_c$  represents the quasi-static uniaxial compressive strength.  $p^* = p/f'_c$  denotes the normalized pressure,  $p$  is the real pressure.  $\dot{\epsilon}^* = \dot{\epsilon}/\dot{\epsilon}_0$  represents the dimensionless strain rate,  $\dot{\epsilon}$  is the real strain rate and  $\dot{\epsilon}_0$  is the reference strain rate.  $A$ ,  $B$ ,  $N$ ,  $C$  and  $S_{\max}$  are normalized cohesive strength, normalized pressure hardening coefficient, pressure hardening exponent, strain rate coefficient and normalized maximum strength, respectively.  $D$  is an index describing the material damage in the range of  $0 \sim 1$ . According to the original HJC model [Holmquist, Johnson, and Cook (1993)], an accumulated damage failure model, also known as compression-shear damage, is considered, which is written as

$$D_c = \sum \frac{\Delta \epsilon_p + \Delta \mu_p}{D_1(p^* + T^*)^{D_2}} \quad (57)$$

317 where  $D_c$  denotes the compression-shear damage parameter,  $\Delta \epsilon_p$  and  $\Delta \mu_p$  denote  
318 the equivalent plastic strain and plastic volumetric strain, respectively.  $D_1$  and  $D_2$   
319 are the damage constants. In order to allow for a finite amount of plastic strain  
320 to fracture, a third damage constant  $E_{f \min}$  is provided.  $T^* = T/f'_c$  denotes the  
321 normalized maximum tensile hydrostatic pressure.

However, the tensile damage of concrete is not considered in the original HJC model. The tensile behavior of concrete is simply considered through maximum tensile hydrostatic pressure. A new brittle tensile failure model based on micro cracking growth of concrete was presented by Jiang similarly as the metal brittle tensile failure [Jiang (2010)]. According to this model, every crack can be

viewed as a sphere cavity zones with the maximum diameter of crack which is called "equivalent micro holes". This model can be formulized as

$$\dot{D}_t = aD_t(1 - D_t)\left(\frac{\sigma_s}{\sigma_0} - 1\right)^\gamma \quad (58)$$

322 where  $a$  is damage factor of micro-crack growth, or frequency of micro-crack  
 323 growth,  $\sigma_0$  is threshold stress of damage development involving micro voids' nu-  
 324 cleation and growth,  $\gamma$  is dependent coefficient of the ultra threshold stress. When  
 325 the tensile damage reaches the limit of damage, spall of material will occur. Con-  
 326 sidering high pressures and air voids, the equation of state (EOS) in HJC model  
 327 is divided into three response regions including linear elastic zone, transition zone  
 328 and full dense zone. More details can be found in papers [Lian, Zhang, Zhou, and  
 329 Ma (2011); Holmquist, Johnson, and Cook (1993)].

#### 330 4.4 Soil model

The soil in this work is modeled by Drucker-Prager constitutive model [Itasca (2005)]. It is made up by shear failure and tension failure. For judging the shear failure region and tension failure region, function  $h(\sigma_m, \tau)$  is defined as

$$h = \tau - \tau^p - \alpha^p(\sigma_m - \sigma^t) \quad (59)$$

where  $\tau = \sqrt{J_2}$  is the effective shear stress and  $J_2$  denotes the second stress invari-  
 ant.  $\sigma_m = I_1/3$  is the spheric stress and  $I_1$  denotes the first stress invariant.  $\tau^p$  and  
 $\alpha^p$  are constants and can be defined as

$$\tau^p = k_\phi - q_\phi \sigma^t \quad (60)$$

$$\alpha^p = \sqrt{1 + q_\phi^2} - q_\phi \quad (61)$$

where  $\sigma^t$  is the tensile strength,  $k_\phi$  and  $q_\phi$  are material constants which can be  
 obtained from the cohesion and frictional angle. When  $h > 0$ , shear failure is em-  
 ployed and the yield function can be described as

$$f^s = \tau + q_\phi \sigma_m - k_\phi \quad (62)$$

If  $h < 0$ , tension failure is employed and yield function can be described as

$$f^t = \sigma_m - \sigma^t \quad (63)$$

331 The parameters of soil are taken from [Luccioni and Luege (2006)] as  $\rho = 1200$   
 332  $\text{kg/m}^3$ ,  $E = 100\text{MPa}$  and  $\varepsilon = 0.3$ . The cohesion is  $0.11\text{MPa}$  and the internal fric-  
 333 tion angle is  $20^\circ$ .

### 334 4.5 Steel model

The Johnson-Cook material model [Johnson and Cook (1983)] is employed in the numerical example to describe the property of the steel plate. The model accounts for the strain rate effect and has widely used to model the behavior of metal during impact and explosion. The yield stress is given by

$$\sigma_y = (A + B\varepsilon^n)(1 + C\ln\dot{\varepsilon}^*)(1 - T^{*m}) \quad (64)$$

335 where  $\varepsilon$  is the equivalent plastic strain,  $\dot{\varepsilon}^* = \dot{\varepsilon}/\dot{\varepsilon}_0$  is the dimensionless plastic  
 336 strain rate with  $\dot{\varepsilon}_0 = 1s^{-1}$ .  $T^* = (T - T_{\text{room}})/(T_{\text{melt}} - T_{\text{room}}) \in [0, 1]$  is the dimen-  
 337 sionless temperature.  $T$  is the material's temperature,  $T_{\text{room}}$  is the room temper-  
 338 ature, and  $T_{\text{melt}}$  is the material's melting temperature. The material constants are  
 339 taken from the reference [Neuberger, Peles, and Rittel (2007)] to be  $A = 950\text{MPa}$ ,  
 340  $B = 560\text{MPa}$ ,  $n = 0.26$ ,  $C = 0.014$  and  $m = 1$ .

The pressure of steel is updated by the Mie-Grüneisen EOS as

$$p = p_H\left(1 - \frac{\gamma\mu}{2}\right) + \gamma\rho E \quad (65)$$

where

$$p_H = \begin{cases} \rho_0 C_0^2 [\mu + (2S - 1)\mu^2 + (S - 1)(3S - 1)\mu^3] & \mu > 0 \\ \rho_0 C_0^2 \mu & \mu < 0 \end{cases} \quad (66)$$

341 The subscript H refers to the Hugoniot curve and  $\mu = \rho/\rho_0 - 1$  is used to represent  
 342 the compression of solid with  $\rho_0$  being the stress-free solid density. Moreover,  $\gamma$ ,  
 343  $C_0$  and  $S$  are the material constants which are taken as  $\gamma = 2.17$ ,  $C_0 = 4569\text{m/s}$  and  
 344  $S = 1.49$  for the numerical example in this paper.

## 345 5 Numerical examples

346 The three dimensional CFDMP scheme has been implemented in our 3D explicit  
 347 material point method code, MPM3D [Ma, Zhang, and Huang (2010)], to solve HE  
 348 air explosion problems. Five numerical examples are presented in this section to  
 349 validate the scheme and demonstrate its capabilities.

### 350 5.1 One-dimensional Shock tube problem

351 Sod shock tube problem [Sod (1978)] is a benchmark for validating codes for  
 352 compressible fluid, so it is taken to demonstrate the FDM solver in CFDMP. As  
 353 shown in Fig. 5, this problem consists of a shock tube with a diaphragm sep-  
 354 arating two regions whose initial states are  $\rho_{\text{left}} = 1.0\text{g/mm}^3$ ,  $p_{\text{left}} = 1.0\text{MPa}$ ,

355  $\rho_{\text{right}} = 0.125\text{g/mm}^3$  and  $p_{\text{right}} = 0.1\text{MPa}$ . The fluids in both regions are initially  
 356 at rest. At time  $t = 0\text{ms}$ , the diaphragm is ruptured. Then, the shock and the  
 357 contact interface travel at different speeds. The results are usually examined at  
 358  $t = 0.143\text{ms}$  when the shock has traveled a distance of about  $0.25\text{mm}$ . This prob-  
 359 lem is employed to test the capability of the FDM solver in CFDMP on simulating  
 360 compressible fluid and does not involve coupling between FDM and MPM. The  
 361 profiles of density, velocity and pressure are plotted in Fig.6 for a grid with 1000  
 362 cells, which shows that the FDM solver's results are in excellent agreement with  
 363 the analytical results. The simulation results obtained by MPM using the same cells  
 364 are also plotted in the figures in which obvious numerical oscillations can be noted.  
 365 Generalized interpolation material point method (GIMP) [Bardenhagen and Kober  
 366 (2004)] can effectively inhibit the numerical oscillations and get better results than  
 367 MPM, however, more computational resources are needed. Unlike the MPM and  
 368 GIMP in which both the particles and background grid are created, the FDM solver  
 369 in CFDMP method updates the variables only in the cell-center points. In this re-  
 370 gard, the CPU times consumed by GIMP and MPM are 78s and 52s, respectively,  
 371 while FDM only takes 46s. Furthermore, the convergence properties of FDM and  
 372 GIMP are studied by plotting the global error norms of the results against the back-  
 373 ground cell length ( $h$ ), as shown in Fig. 7. The convergence rate of FDM is about  
 374 50% higher than that of GIMP. What's more, the global errors of FDM using 500  
 375 cells are almost equal to that of GIMP using 1000 cells, which demonstrates the ra-  
 376 tionality of employing FDM to simulate the fluid region which contain shock wave  
 377 propagation in HE problems in CFDMP.

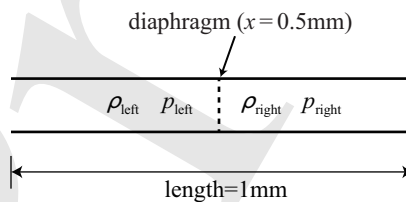


Figure 5: 1D shock tube problem

## 378 5.2 Two-dimensional HE explosion and interaction with a concrete slab

379 A two-dimensional HE explosion problem is simulated as shown in Fig. 8. A  
 380 HE charge with a radius of 50mm detonates and drives the surrounding air to  
 381 interact with a concrete slab. The HE and surrounding air are simulated by the  
 382 high explosive model and air model presented in Section 4 and the boundary con-  
 383 ditions of the fluid region are all "flow out". The concrete is simulated by the

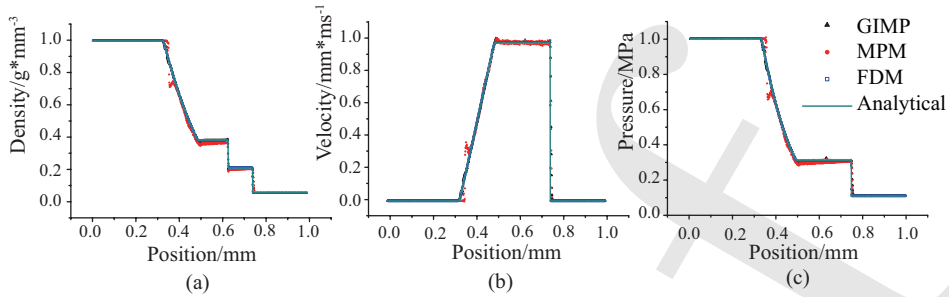


Figure 6: Profiles of density, velocity and pressure obtained by analytical solution, MPM, GIMP and FDM

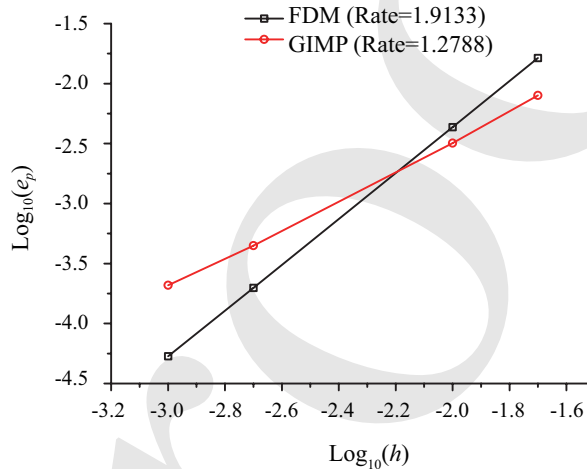


Figure 7: Pressure convergence curves

384 concrete model with tensile damage presented in Section 4. The computational  
 385 domain  $(-180, 160\text{mm}) \times (0, 500\text{mm})$  is divided into FDM region (Fluid region)  
 386 of  $(-180, 120\text{mm}) \times (0, 500\text{mm})$  and MPM region (Interaction region) of  $(110,$   
 387  $160\text{mm}) \times (0, 500\text{mm})$ , as shown in Fig. 8. All regions are discretized by square  
 388 cells of side length 2 mm. The bridge region is  $(110, 120\text{mm}) \times (0, 500\text{mm})$  and  
 389  $w = 5$ , i.e., the width of the bridge region is equal to 5 times of the cell's side length.  
 390 The center of the HE charge is located at  $(0, 250)$ .

391 Fig.9 shows the colored contours of the pressure at  $20\mu\text{s}$  in FDM and MPM region  
 392 respectively. It can be recognized that the wave propagation transport through the  
 393 bridge region correctly. To quantitatively demonstrate that CFDMP does not in-

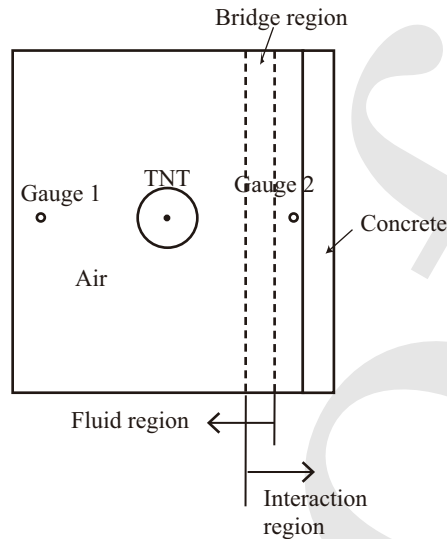


Figure 8: Computational regions of 2D HE explosion

394 introduce obvious interface effect, the pressure time history of two symmetric gauge  
 395 points in the air, which have the same distance from the center of the HE charge  
 396 (see Fig. 8), are shown in Fig.10. The gauge 1  $(-125, 250)$  is in the FDM region  
 397 while the gauge 2  $(125, 250)$  is in MPM region. The pressure time histories of  
 398 the two gauge points are in good agreement, which demonstrates that the proposed  
 399 coupling method between FDM and MPM works very well.

400 To further study the effects of the width of the bridge region, Fig.11 plots the pres-  
 401 sure time histories for  $w$  equals to 2 and 8, respectively, which shows that the bridge  
 402 region would smooth the shock wave excessively when  $w$  is too large. Therefore,  
 403 the width of the bridge region should not be too large, and  $w = 5$  performs very  
 404 well as shown in Fig.10.

405 The pressures in the interaction region obtained by MPM and CFDMP are com-  
 406 pared in Fig. 12. Not only the time step used in MPM simulation is much smaller  
 407 than that of CFDMP due to some particles with extraordinary high speed near the  
 408 contact discontinuity, but also the MPM result suffers more numerical oscillations.  
 409 Besides, MPM requires more memory because it places particles in the whole re-  
 410 gion. As a result, the total computational time of MPM is 181 minutes 9 seconds,  
 411 while the total computational time for CFDMP is only 50 minutes 30 seconds.

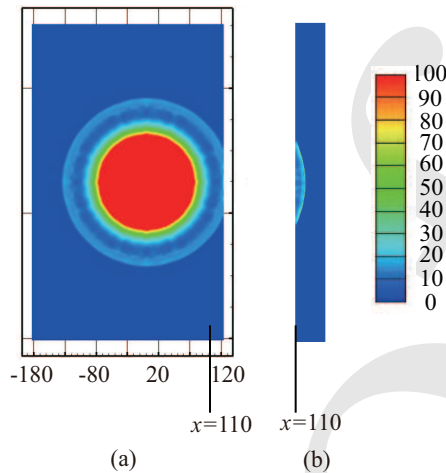


Figure 9: Contours of pressure at  $t = 20\mu s$ . (a). FDM region; (b). MPM region

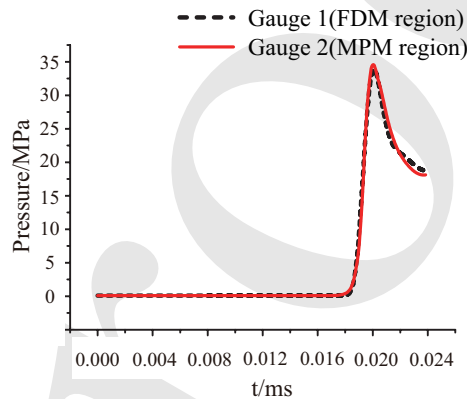


Figure 10: Time history of the pressures at two gauge points of the same distance

### 412 5.3 Three-dimensional HE explosion and interaction with a concrete slab

413 To validate the capability of CFDMP in simulating HE explosion problem and the  
 414 damage effect to the structure nearby, a concrete slab under blast loads experi-  
 415 ment [Luccioni and Luege (2006)] is studied. The geometrical configuration of the  
 416 experiment and the load locations are shown in Fig.13. Spherical HE charges of  
 417 5Kg (TNT equivalent mass of 4Kg) and 12.5Kg (TNT equivalent mass of 10Kg)  
 418 of Gelamon VF80 were employed placed at 0.5m height above the top surface of  
 419 the slab as shown in Fig.13(a). There were three tests on the same slab succes-  
 420 sively, the first produced a fracture parallel to the short side, so for the following

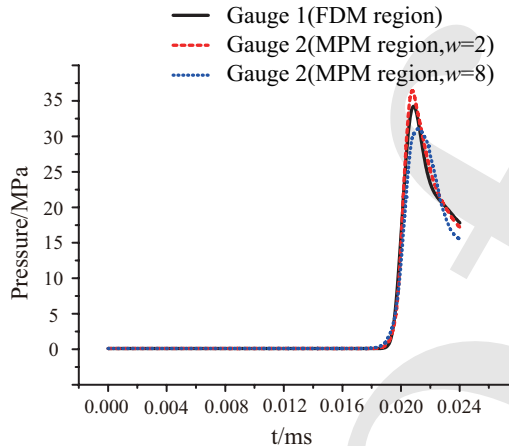


Figure 11: Time history of the pressures at two gauge points of the same distance (different width of the bridge region)

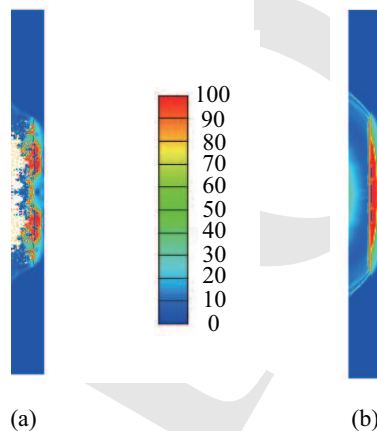


Figure 12: Contours of pressure in interaction region at  $t = 32.5 \mu s$ . (a). MPM; (b). CFDMP

421 detonations, the original slab behaved as two square independent slabs so we sim-  
 422 ulate two tests independently. The average compressive strength of the concrete  
 423 (25MPa) was obtained from compression tests with the same concrete as the slab.  
 424 In [Luccioni and Luege (2006)], AUTODYN was used to simulate the experiments,  
 425 and their material parameters are used in our simulations. In both AUTODYN and  
 426 our simulations, a remap method is used to map the 1D simulation results of the

427 detonation process to 3D region as the initial condition in the FDM region and then  
 428 simulate the propagation of blast wave in air by 3D code.

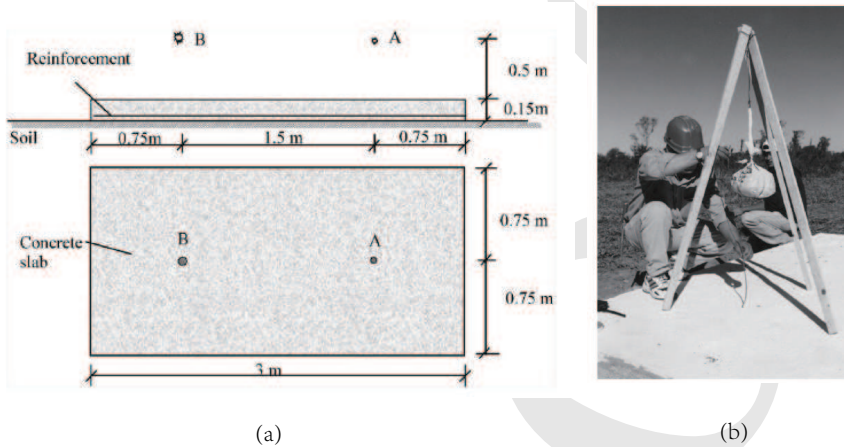


Figure 13: (a). Concrete slab dimensions and charge positions; (b). Placement of the explosive charge suspended above slab [Luccioni and Luege (2006)]

In the experiment, the charges of 5Kg and 12.5Kg Gelamon produced the crushing of concrete in a circular zone of about 250mm and 300mm diameter, respectively. Hereby, Luccioni et al. [Luccioni and Luege (2006)] overfitted an empirical formula for the estimation of explosive charges from crushing diameters or crushing dimensions from explosive charges as

$$\ln(3.63D/h) = 0.1838(W^{1/3}/h) \quad (67)$$

429 where  $D$  is the diameter of the crushing zone and  $h$  is the height of the charge from  
 430 the concrete slab.  $W$  denotes the TNT equivalent mass of the charge.

431 In order to reproduce the crushing or disintegration of the concrete and counteract  
 432 the great distortion that can cause excessive deformation of the mesh, erosion was  
 433 used in [Luccioni and Luege (2006)]. Profit from MPM's ability to deal with the  
 434 large deformation problems, we use CFDMP to simulate this test without use of  
 435 the erosion model. The particles fail when their damage value reaches unit. Fig.  
 436 14 shows the numerical results for the test of 5Kg charge obtained by CFDMP, in  
 437 which (a) is the failure area on the front of the slab and (b) is the tensile damage  
 438 on the back of the slab. The diameter of the crushing area is about 261mm and the  
 439 damage on the back of the slab expands from the center to the surrounding radially  
 440 which conforms to the analysis in [Luccioni and Luege (2006)].

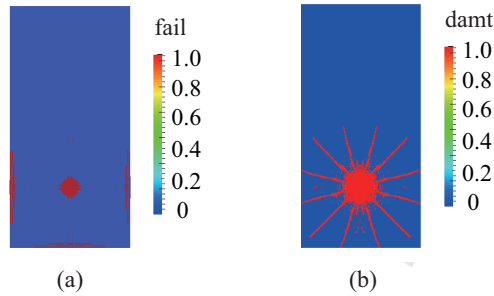


Figure 14: Numerical results for 5Kg charge test. (a). Concrete crushing area on the front of the slab; (b). Tensile damage on the back of the slab

441 To compare the CFDMP results with those obtained from the experiment and the  
 442 empirical formula (67), we conducted a series of numerical tests with TNT equiv-  
 443 alent mass of 2Kg, 4Kg, 10Kg and 20Kg. The results are plotted in Fig.15. For the  
 444 cases of 4Kg and 10Kg, the numerical results are in good agreement with those ob-  
 445 tained by the experiment and the empirical formula. For the case of 2Kg and 20Kg,  
 446 the crushing regions also agree well with the prediction of the empirical formula.

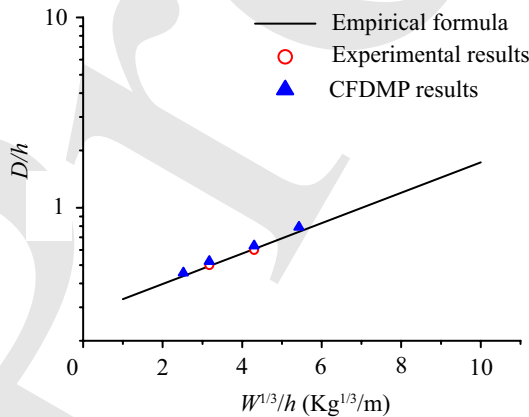


Figure 15: Relative diameter of the crushing zone  $D/h$  as a function of the inverse of the scaled distance  $W^{1/3}/h$

#### 447 5.4 Response of steel plates subjected to air-blast loading

448 Understanding the dynamic behavior of blast loaded armor steel plates is a key to  
 449 design a protection structure successfully. A series of experiments and numerical  
 450 calculations were carried out by Neuberger et. al. [Neuberger, Peles, and Rittel  
 451 (2007)] to study the scaling characteristics of the dynamic response of circular RHA  
 452 steel plates to large bare spherical air blast. As shown in Fig.16(a), the target plate  
 453 was supported by two thick armor steel plates with circular holes. The spherical  
 454 TNT charges were hanged in air using fisherman's net and were ignited from the  
 455 center of the charge. The numerical model is shown in Fig.16(b), in which the  
 456 charge's weight is  $W$ , distance from the plate's surface to the center of the charge is  
 457  $R$ , plate thickness is  $t$  and diameter is  $D$ , all of them are variables in the tests. The  
 458 maximum deflection of the plate  $\delta$  is measured during the experiments. Steel, TNT  
 459 and air are simulated by the material models presented in Section 4. Two series of  
 460 cases are simulated, and the experimental and numerical parameters are listed in  
 461 Tab. 1. The normalized peak deflection,  $\delta/t$ , obtained by CFDMP are compared  
 462 with those obtained by the experiments and LS-DYNA in Tab. 2.

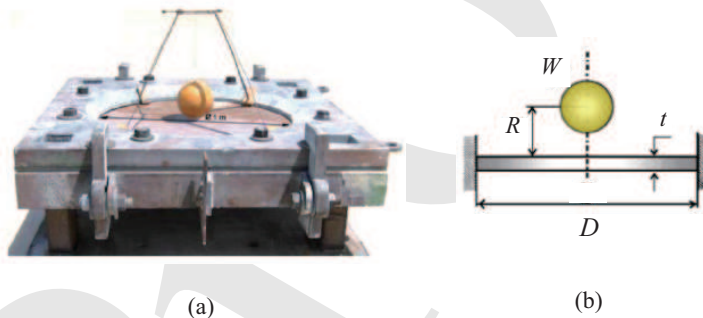


Figure 16: (a). Experimental setup [Neuberger, Peles, and Rittel (2007)]; (b). The numerical model

463 For series 1 (cases 1, 2 and 3), which represents a charge of 30Kg TNT for the  
 464 full scale prototype, the structural response is mostly dynamic elastic. The first two  
 465 cases show that the experimental and numerical results are in excellent agreement  
 466 and the scaling are hardly affected by the varying the geometry scale as stated in  
 467 [Neuberger, Peles, and Rittel (2007)]. The third case is the numerical result of the  
 468 full scale problem given by CFDMP, it proves the conclusion again.

469 For series 2 (cases 4, 5 and 6), which represents a charge of 70Kg TNT for the  
 470 full scale prototype, the increasing plastic strains arise in the structural dynamic

Table 1: Experimental and numerical cases

case	scaling factor	$t$ (m)	$D$ (m)	$W$ (Kg TNT)	$R$ (m)
1	4	0.01	0.5	0.468	0.1
2	2	0.02	1	3.75	0.2
3	1(full scale)	0.04	2	30	0.4
4	4	0.01	0.5	1.094	0.1
5	2	0.02	1	8.75	0.2
6	1(full scale)	0.04	2	70	0.4

Table 2: Normalized peak deflection  $\delta/t$ 

case	scaling factor	Experiment	CFDMP	LS-DYNA
1	4	2.60	2.69	2.59
2	2	2.70	2.71	2.62
3	1(full scale)		2.68	
4	4	4.85	5.2	4.98
5	2	5.35	5.45	5.24
6	1(full scale)		5.625	

471 response. Thus the scaling is affected, as discussed in [Neuberger, Peles, and Rittel  
 472 (2007)]. Case 4 and case 5 show that the experimental and numerical results are in  
 473 good agreement, and the effect on the scaling are also represented. As the scaling  
 474 factor vary approaching to 1, the normalized peak deflection  $\delta/t$  increase, which  
 475 tells the effect on the scaling. The last case is the numerical result of the full scale  
 476 problem obtained by CFDMP, whose normalized peak deflection  $\delta/t$  is the largest  
 477 which conform to the conclusion.

478 Fig.17 shows the final configuration of case 5. The figure obtained by CFDMP is  
 479 similar to the shape of experimental photograph. Fig.18 shows the colored contours  
 480 of the Mises stress at time of 0.3ms, 0.5ms and 1.0ms respectively for case 2 and  
 481 case 5 (the scaling factor are both 2). For case 2, most of the region are in elastic  
 482 period, while a large portion has entered into plastic period for case 5. So the  
 483 scaling of case 5 are affected as discussed in [Neuberger, Peles, and Rittel (2007)].

### 484 5.5 Damage of concrete slab with defect subjected to air-blast loading

485 Based on the examples shown in Section 5.3, we bring a little modification to the  
 486 slab to illustrate the ability of CFDMP to solve the strong FSI problem for more  
 487 complex geometry structure. As shown in Fig. 19(a), in a block region right against  
 488 the center of the HE charge (the red region), the concrete slab is weakened by



Figure 17: Final configuration of case 5. (a). Experimental photograph; (b). CFDMP

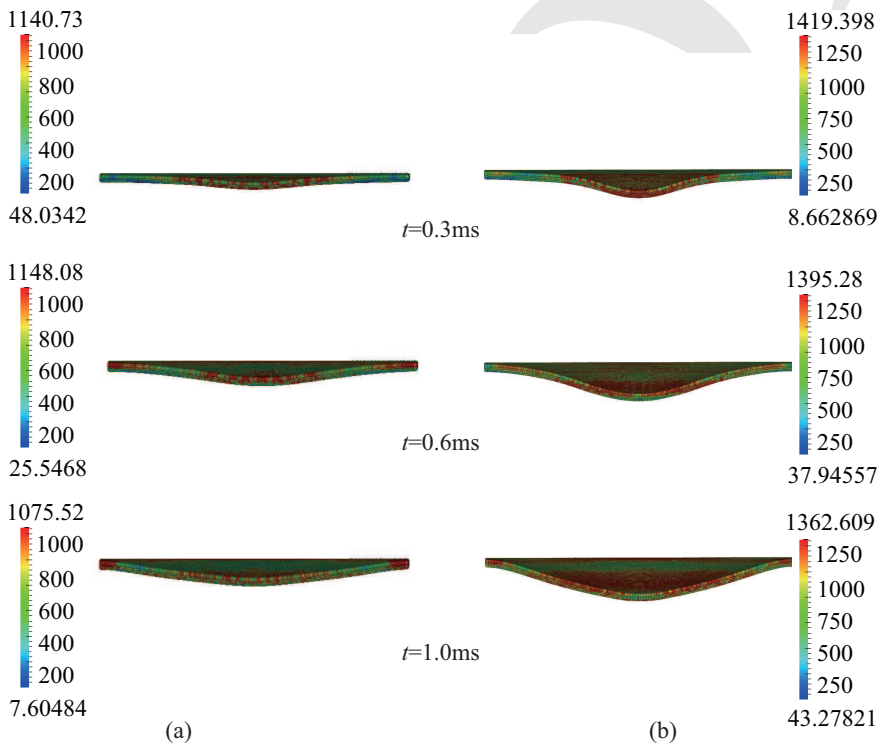


Figure 18: Mises stress. (a). case 2; (b). case 5

489 reducing its thickness from 0.15m to 0.02m so as to simulate the effect of the defect  
 490 in the slab, other conditions are the same as those in Section 5.3 (5Kg charge). The  
 491 tensile damage in the back of the slab is presented in Fig. 19(b). All the defect  
 492 region is crushed and the damage region of the slab is larger than that of the slab  
 493 without defect shown in Fig. 14. Besides, the damage shape of the two case are

494 also different. The damage shape of the slab without defect is expanded from the  
 495 center to the surrounding radially while the damage shape of the slab with defect is  
 496 annular around the center.

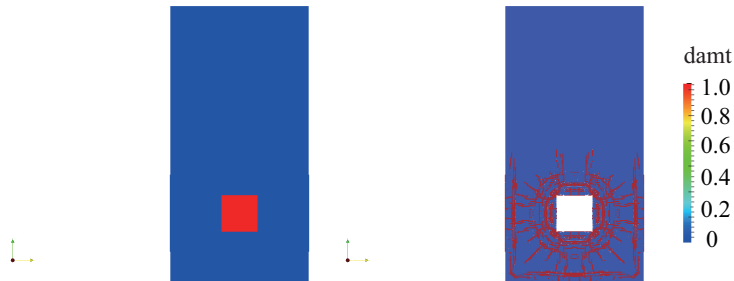


Figure 19: (a). Initial condition; (b). The tensile damage in the back of the slab

## 497 6 Conclusion

498 A coupled finite difference material point (CFDMP) method is proposed through  
 499 the bridge region to combine the advantages of FDM and MPM in this paper. It  
 500 uses an Eulerian frame in the fluid region and a Lagrangian frame in the FSI re-  
 501 gion. FDM is employed in the Eulerian frame, while MPM is employed in the  
 502 Lagrangian frame. So the region involving shock wave dispersion problem is sim-  
 503 ulated by FDM whereas the region involving history dependent materials and FSI is  
 504 simulated by MPM. In this way, the advantages of FDM and MPM are fully utilized  
 505 in different regions of the problem. Both shock tube problem and 2D HE explosion  
 506 simulation have verified the accuracy and efficiency of this algorithm. CFDMP is  
 507 applied to simulate the dynamic responses of concrete slab and steel slab under air  
 508 blast loading, whose numerical results coincide to the available experimental results  
 509 and the conclusion reported in literature. Therefore the proposed CFDMP method  
 510 provides a powerful numerical tool for the study of explosion problems. What's  
 511 more, the methodology can be generalized to combine other methods which are  
 512 based on different frames of reference.

513 **Acknowledgement:** Supported by the National Basic Research Program of China  
 514 (2010CB832701), National Natural Science Foundation of China (11390363), Spe-  
 515 cialized Research Fund for the Doctoral Program of Higher Education (SRFDP) of  
 516 Chinese Ministry of Education (20130002110078) and Tsinghua University Initia-  
 517 tive Scientific Research Program.

518 **References**

- 519 **Aktay, L.; Johnson, A. F.** (2007): FEM/SPH coupling technique for high velocity  
520 impact simulations. *Advances in Meshfree Techniques*, pp. 147–167.
- 521 **Banerjee, B.** (2004): Material point method simulations of fragmenting cylinders.  
522 In *17th Engineering Mechanics Conference*.
- 523 **Bardenhagen, S. G.; Kober, E. M.** (2004): The generalized interpolation material  
524 point method. *Computer Modeling in Engineering and Sciences*, vol. 5(6), pp.  
525 477–495.
- 526 **Benson, D. J.** (1992): Computational methods in Lagrangian and Eulerian hy-  
527 drocodes. *Computer Methods in Applied Mechanics and Engineering*, vol. 99(2-3),  
528 pp. 235–394.
- 529 **Brackbill, J. U.; Ruppel, H. M.** (1986): Flip: a method for adaptively zoned,  
530 particle-in-cell calculations in two dimensions. *Journal of Computational Physics*,  
531 vol. 65, pp. 314–343.
- 532 **Cockburn, B.; Hou, S.; Shu, C. W.** (1990): Tvb runge-kutta local projection  
533 discontinuous galerkin finite element method for scalar conservation laws iv: The  
534 multidimensional case. *Math Comp*, vol. 54, pp. 545–581.
- 535 **Cui, X. X.; Zhang, X.; Sze, K. Y.; Zhou, X.** (2013): An alternating finite differ-  
536 ence material point method for numerical simulation of high explosive explosion  
537 problems. *Computer Modeling in Engineering and Sciences*, vol. 92(5), pp. 507–  
538 538.
- 539 **Fairlie, G.; Bergeron, D.** (2002): Numerical simulation of mine blast loading on  
540 structures. In *17th Military Aspects of Blast Symposium*.
- 541 **Flekkoy, E. G.; Wagner, G.; Feder, J.** (2000): Hybrid model for combined  
542 particle and continuum dynamics. *Europhysics Letters*, vol. 52(3), pp. 271–276.
- 543 **Gilmanov, A.; Acharya, S.** (2008): A hybrid immersed boundary and material  
544 point method for simulating 3d fluid-structure interaction problems. *International*  
545 *Journal for Numerical Methods in Engineering*, vol. 56, pp. 2151–2177.
- 546 **Guilkey, J.; Harman, T.; Banerjee, B.** (2007): An Eulerian Lagrangian approach  
547 for simulating explosions of energetic devices. *Computers and Structures*, vol. 85,  
548 pp. 660–674.
- 549 **Hallquist, J. O.** (1998): *LS-DYNA Theoretical Manual*. Livermore Software  
550 Technology Corporation.
- 551 **Holmquist, T. J.; Johnson, G. R.; Cook, W. H.** (1993): A computational con-  
552 stitutive model for concrete subjected to large strains, high strain rates, and high  
553 pressures. In *14th International Symposium on Ballistics Quebec, Canada*.

- 554 **Hu, W.; Chen, Z.** (2006): Model-based simulation of the synergistic effects of  
555 blast and fragmentation on a concrete wall using the MPM. *International Journal*  
556 *of Impact Engineering*, vol. 32, pp. 2066–2096.
- 557 **Itasca** (2005): FLAC-Fast Lagrangian Analysis of Continua User's Manual (Ver-  
558 sion 5.0). In *Itasca Consulting Group Inc.*
- 559 **Jacinto, A. C.; Ambrosini, R. D.; Danesi, R. F.** (2001): Experimental and  
560 computational analysis of plates under air blast loading. *International Journal of*  
561 *Impact Engineering*, vol. 25, pp. 927–947.
- 562 **Jiang, D.** (2010): *Study on chracterization of damage evolution and failure law*  
563 *of engineering materials*. PhD thesis, University of Science and Technology of  
564 China, 2010.
- 565 **Johnson, G. R.; Cook, W. H.** (1983): A constitutive model and data for metals  
566 subjected to large strains, high strain rates and high temperatures. In *7th Inter-*  
567 *national Symposium on Ballistics, The Hague, Netherlands: American Defense*  
568 *Preparedness Association*, pp. 541–547.
- 569 **Lax, P. D.; Wendroff, B.** (1964): Difference scheme for hyperbolic equations  
570 with high order of accuracy. *Communications on Pure and Applied Mathematics*,  
571 vol. 17, pp. 381–398.
- 572 **Lian, Y. P.; Zhang, X.; Liu, Y.** (2012): An adaptive finite element material point  
573 method and its application in extreme deformation problems. *Computer Methods*  
574 *in Applied Mechanics and Engineering*, vol. 241-244 (1), pp. 275–285.
- 575 **Lian, Y. P.; Zhang, X.; Zhou, X.; Ma, S.; Zhao, Y. L.** (2011): Numerical  
576 simulation of explosively driven metal by material point method. *International*  
577 *Journal of Impact Engineering*, vol. 38, pp. 238–246.
- 578 **Lian, Y. P.; Zhang, X.; Zhou, X.; Ma, Z. T.** (2011): A femp method and  
579 its application in modeling dynamic response of reinforced concrete subjected to  
580 impact loading. *Comput. Methods Appl. Mech. Engrg.*, vol. 200, pp. 1659–1670.
- 581 **Liu, G. R.; Liu, M. B.** (2003): *Smoothed particle hydrodynamics: a meshfree*  
582 *particle method*. World Scientific, Singapore.
- 583 **Liu, M. B.; Liu, G. R.; Lam, K. Y.; Zong, Z.** (2003): Meshfree particle simula-  
584 tion of the detonation process for high explosives in shaped charge unlined cavity  
585 configurations. *Shock Waves*, vol. 12(6), pp. 509–520.
- 586 **Liu, M. B.; Liu, G. R.; Lam, K. Y.; Zong, Z.** (2003): Smoothed particle  
587 hydrodynamics for numerical simulation of underwater explosion. *Computational*  
588 *Mechanics*, vol. 30, pp. 106–118.

- 589 **Liu, M. B.; Liu, G. R.; Zong, Z.; Lam, K. Y.** (2003): Computer simulation  
590 of high explosive explosion using smoothed particle hydrodynamics methodology.  
591 *Computers and Fluids*, vol. 32, pp. 305–322.
- 592 **Liu, W. K.; Belytschko, T.; Chang, H.** (1986): An arbitrary lagrangian-eulerian  
593 finite element method for path-dependent materials. *Computer Methods in Applied*  
594 *Mechanics and Engineering*, vol. 58, pp. 227–245.
- 595 **Luccioni, B. M.; Ambrosini, R. D.; Danesi, R. F.** (2004): Analysis of building  
596 collapse under blast loads. *Engineering Structures*, vol. 26, pp. 63–71.
- 597 **Luccioni, B. M.; Luege, M.** (2006): Concrete pavement slab under blast loads.  
598 *International Journal of Impact Engineering*, vol. 32, pp. 1248–1266.
- 599 **Lucy, L. A.** (1977): A numerical approach to the testing of the fission hypothesis.  
600 *Astrophysical Journal*, vol. 82, pp. 1013–1024.
- 601 **Ma, J.; Hanan, J. C.; Komanduri, R.; Lu, H.** (2012): Simulation of the de-  
602 formation mechanisms of bulk metallic glass (BMG) foam using the material point  
603 method. *Computer Modeling in Engineering and Sciences*, vol. 86(4), pp. 349–  
604 382.
- 605 **Ma, S.; Zhang, X.; Lian, Y. P.; Zhou, X.** (2009): Simulation of high explosive  
606 explosion using adaptive material point method. *Computer Modeling in Engineer-*  
607 *ing and Sciences*, vol. 39(2), pp. 101–123.
- 608 **Ma, S.; Zhang, X.; Qiu, X. M.** (2009): Comparison study of MPM and SPH in  
609 modeling hypervelocity impact problems. *International Journal of Impact Engi-*  
610 *neering*, vol. 36, pp. 272–282.
- 611 **Ma, T. B.; Wang, C.; Ning, J. G.** (2008): Multi-material Eulerian formulations  
612 and hydrocode for the simulation of explosions. *Computer Modeling in Engineer-*  
613 *ing and Sciences*, vol. 33(2), pp. 155–178.
- 614 **Ma, Z. T.; Zhang, X.; Huang, P.** (2010): An object-oriented mpm framework  
615 for simulation of large deformation and contact of numerous grains. *Computer*  
616 *Modeling in Engineering & Sciences*, vol. 55(1), pp. 61–88.
- 617 **Neuberger, A.; Peles, S.; Rittel, D.** (2007): Scaling the response of circular plates  
618 subjected to large and close-range spherical explosions. part i: Air-blast loading.  
619 *International Journal of Impact Engineering*, vol. 34, pp. 859–873.
- 620 **Ning, J. G.; Chen, L. W.** (2004): Fuzzy interface treatment in eulerian method.  
621 *Science in China Series E-Engineering and Materials Science*, vol. 47(5), pp. 550–  
622 568.
- 623 **Osher, S.; Fedkiw, R. P.** (2001): Level set methods: an overview and some recent  
624 results. *Journal of Computational Physics*, vol. 169, pp. 463–502.

- 625 **Sod, G. A.** (1978): A survey of several finite difference methods for systems of  
626 nonlinear hyperbolic conservation laws. *Journal of Computational Physics*, vol.  
627 27, pp. 1–31.
- 628 **Sulsky, D.; Chen, Z.; Schreyer, H. L.** (1994): A particle method for history-  
629 dependent materials. *Computer Methods in Applied Mechanics and Engineering*,  
630 vol. 118(1-2), pp. 179–196.
- 631 **Sulsky, D.; Zhou, S. J.; Schreyer, H. L.** (1995): Application of a particle-in-cell  
632 method to solid mechanics. *Computer Physics Communications*, vol. 87(1-2), pp.  
633 236–252.
- 634 **Wang, C.; Zhang, X. X.; Shu, Q. W.; Ning, J. G.** (2012): Robust high order dis-  
635 continuous Galerkin schemes for two-dimensional gaseous detonations. *Journal*  
636 *of Computational Physics*, vol. 231, pp. 653–665.
- 637 **Wu, C. Q.; Hao, H.** (2005): Modeling of simultaneous ground shock and airblast  
638 pressure on nearby structures from surface explosions. *International Journal of*  
639 *Impact Engineering*, vol. 31, pp. 699–717.
- 640 **Xu, K.; Lu, Y.** (2006): Numerical simulation study of spallation in reinforced  
641 concrete plates subjected to blast loading. *Computers and Structures*, vol. 84, pp.  
642 431–438.
- 643 **Yanenko, N. N.** (1971): *The method of fractional steps*. Springer-Verlag.
- 644 **Youngs, D. L.** (1982): Time dependent multi-material flow with large fluid distur-  
645 bance. *Numerical Methods for Fluid Dynamics*, pp. 273–285.
- 646 **Zhang, D. L.** (2010): *A course in computational fluid dynamics*. Higher Educa-  
647 tion Press.
- 648 **Zhang, D. Z.; Ma, X.; Giguere, P. T.** (2011): Material point method enhanced by  
649 modified gradient of shape function. *Journal of Computational Physics*, vol. 230,  
650 pp. 6379–6398.
- 651 **Zhang, D. Z.; Zou, Q.; VanderHeyden, W. B.; Ma, X.** (2008): Material point  
652 method applied to multiphase flows. *Journal of Computational Physics*, vol. 227,  
653 pp. 3159–3173.
- 654 **Zhang, X.; Sze, K. Y.; Ma, S.** (2006): An explicit material point finite element  
655 method for hyper-velocity impact. *International Journal for Numerical Methods*  
656 *in Engineering*, vol. 66, pp. 689–706.
- 657 **Zhang, Y. J.; Xu, S. L.** (2007): Numerical simulation on flow-structure interac-  
658 tion loaded by a blast wave from a central charge. *Journal of University of Science*  
659 *and Technology of China*, vol. 37, pp. 6–12.
- 660 **Zukas, J.; Walters, W.** (1998): *Explosive effects and applications*. Springer.

Proof